

Implementation of nozzle motion for material extrusion additive manufacturing in Ansys Fluent

Max Galloway, Sung Hin Lam, Hoda Amel, Robert Richardson, Robert Kay & Masoud Jabbari

To cite this article: Max Galloway, Sung Hin Lam, Hoda Amel, Robert Richardson, Robert Kay & Masoud Jabbari (2024) Implementation of nozzle motion for material extrusion additive manufacturing in Ansys Fluent, *Virtual and Physical Prototyping*, 19:1, e2397816, DOI: [10.1080/17452759.2024.2397816](https://doi.org/10.1080/17452759.2024.2397816)

To link to this article: <https://doi.org/10.1080/17452759.2024.2397816>



© 2024 The Author(s). Published by Informa UK Limited, trading as Taylor & Francis Group



Published online: 02 Sep 2024.



Submit your article to this journal [↗](#)



Article views: 361



View related articles [↗](#)



View Crossmark data [↗](#)

Implementation of nozzle motion for material extrusion additive manufacturing in Ansys Fluent

Max Galloway^a, Sung Hin Lam^a, Hoda Amel^b, Robert Richardson ^a, Robert Kay ^a and Masoud Jabbari ^a

^aSchool of Mechanical Engineering, University of Leeds, Leeds, UK; ^bNational Centre for Additive Manufacturing, The Manufacturing Technology Centre, Coventry, UK

ABSTRACT

Most computational fluid dynamics (CFD) modelling of material extrusion additive manufacturing (MEX-AM) mainly relies on a moving boundary condition applied to the print bed and not the direct modelling of the motion of the nozzle. This paper presents step-by-step and detailed implementation of the nozzle motion as well as non-isothermal non-Newtonian flow during MEX-AM in Ansys Fluent. For nozzle motion the overset approach is used for the meshing which allows for the nozzle and the rest of the domain to be meshes separately, streamlining meshing and motion. The method is initially used to simulate a single strand, which was validated against experimental and numerical data. It was then applied to demonstrate out-of-plane nozzle motion in two case studies: three-layer printing and printing on a ramp. The model is further developed to simulate a single strand deposition with the well-known Cross-William-Landel-Ferry (Cross-WLF) behaviour for a thermal and shear-dependent material flow.

ARTICLE HISTORY

Received 11 February 2024
Accepted 22 August 2024

KEYWORDS

MEX-AM; nozzle motion;
overset meshing; CFD



1. Introduction

One of the most attractive solutions is material extrusion additive manufacturing (MEX-AM) which continues to grow in popularity and application across industry due to the low cost of the machinery and wide range of materials it can process [1–3]. The increasing industry attention stems from the processes' ability to potentially provide significant cost savings through decreased manufacturing expenses and shorter production timelines, making MEX-AM an enticing approach for industries such as aerospace [4], automotive [5], energy [6], and healthcare technologies [7].

Manufactured items through MEX-AM typically have poorer mechanical properties than those manufactured with conventional processes which tend to limit the processes' current application areas [8]. Such shortfalls are the consequence of manufacturing process parameters and material behaviour during deposition, and their interplay [9]. As the demand for MEX-AM continues to grow, the need for its improvement becomes more pronounced, necessitating the development of a deeper theoretical understanding [10]. Considerable effort has been dedicated to researching the process through experimental, analytical and numerical work [5,11,12]. Numerical modelling of MEX-AM provide great insight

into the process and have proven to have great predictive abilities. Such model can build a greater understanding manufacturing-induced issues to develop strategies to mitigate such faults and limitations such that the process can become more widespread across industry [10].

Within computational fluid dynamics (CFD) analysis, it is typical to assess the impact of the process parameters on the final strand morphology. Parameters such as nozzle velocity, nozzle height [13,14], temperature [15,16], path planning [17], bounding pressure [18] and rheology [19,20] have been investigated. However, the interaction between strands in numerical models is often neglected and limited to a single-strand deposition [8,10,14,16,17]. Comparatively, there has been a lack of investigation into multi-layer simulations due to the computational complexity this process involves. In part, this is due to the computational expense and intensive labour involved with the dynamics of the moving nozzle, and therefore, changing mesh. There have been implementations of multi-layer simulations [13,18–20]. However these works have their limitations and the proliferation so such approaches niche. Typically in literature, the movement of the nozzle is not modelled directly but rather a moving wall condition is imposed

CONTACT Masoud Jabbari  m.jabbari@leeds.ac.uk  School of Mechanical Engineering, University of Leeds, Leeds LS2 9JT, UK

© 2024 The Author(s). Published by Informa UK Limited, trading as Taylor & Francis Group

This is an Open Access article distributed under the terms of the Creative Commons Attribution License (<http://creativecommons.org/licenses/by/4.0/>), which permits unrestricted use, distribution, and reproduction in any medium, provided the original work is properly cited. The terms on which this article has been published allow the posting of the Accepted Manuscript in a repository by the author(s) or with their consent.

on the printing bed to emulate a relative motion. This method has seen use in [13,15,17,19,21–23]. However, this approach is restricted in application as it cannot be used for multi-layer simulations as the nozzle must move out-of-plane to do this but, the moving substrate method only allows in-plane motion. Furthermore, with this approach, the geometry of the bed must be flat and does not allow for simulations of beds with inclined geometry or gaps so the investigation into these cases cannot be conducted numerically. The inability to print multiple layers with this approach is its biggest drawback as the investigations are limited to single strands which does not allow investigation into layer bounding and the mesostructure which is perhaps the area of greatest interest. This said, in [21] the mesostructure of a multi-layer print was conducted to investigate aligned and skewed depositions of layers and the resulting porosity. This method required multiple meshes, where each strand would form a new boundary for a new mesh. As such, each layer and strand required a new mesh to be created which is a very laborious process. Additionally, this method does not allow for previous strands to be influenced by the new strand which limits the scope of the method as the contact bounding is heavily influenced by this interaction which is indeed noted in [21]. As such this method can never fully capture the interaction between layers and does not allow for the implementation of a non-isothermal process, such as fused filament fabrication (FFF), because of this.

To the authors' knowledge, the implementation of a moving nozzle has only been implemented by Xia et al. [16,24], and a series of works conducted by Spangenberg et al. [22,25,26]. In [16] the FFF process was modelled. This paper utilised a non-isothermal front-tracking/finite volume approach along with a non-Newtonian fluid model to anticipate the shape of filaments, temperature distribution, contact area, and reheat regions when new filaments were placed over previously deposited ones. This model was expanded to include visco-elastic effects in a later paper [24]. However, these papers are mainly a demonstration of the method. While the validation of a two-layer print is said to be compared quantitatively to an analytical model, neither paper includes qualitative or experimental validation. Further to this, analytical models have been found to not accurately reflect the experimental trends [23]. The main limitation of these paper is the lack of clarity on the implementation of the process. No meshing methodology or CFD solver is described which makes the replication of their methodology difficult.

In [22,25,26] the immersed boundary method (IB method) was employed for the modelling of 3D concrete printing (3DCP) using the commercial software FLOW-3D[®]; successfully capturing the geometry of the single [22] and multiple strands [25,26]. The approach showed

promise, with both papers validating their results, demonstrating very close agreement with experimental data and predicting the regions of yield within the extruded material. However, each simulation took several days to complete on a high-performance computer, with the IB method requiring high levels of refinement throughout the whole domain to capture the boundaries of the nozzle within the fluid accurately. The method thus far has only been implemented for large-area printing application, and further evidence that this method is applicable for micro-scale nozzles methods (such as for FFF or direct ink writing) is required. Furthermore, it was noted in [25] that with greater layers numerical instability and inaccuracy develop due to the interpolation around the defined boundary and no more than four layers could be achieved. It is noted in the concluding remarks of [25] that a more computationally robust model is required.

There is a need for a robust process which allows for out-of-plane motion such that multiple layers of the MEX-AM process can be simulated. To achieve this, the use of an appropriate meshing technique will be required to readily allow for mesh motion in a robust, stable and accurate manner. The overset method offers control over the refinement regions within the domain that can move with the nozzle. This approach allows for body-fitted meshes to fully resolve the near-wall flow fields, representing an improvement over the IB method where this is not possible. Furthermore, this approach has benefits regarding the workflow over other approaches as meshes can be reused over cases as the computational domain is built up of separate meshes. For example, a single nozzle mesh can be used across multiple cases. The method does not require re-meshing of the domain but rather just the coupling of the two meshes, while this does incur a computational penalty over fixed boundary due to the interpolations between component and background meshes the provided flexibility of the approach vastly outweighs this. As such, this study aims to develop and present a numerical model where the motion of the nozzle is considered, allowing for a better understanding of MEX-AM and aiding in the development of flexible printing strategies. It is, moreover, the aim of this paper to present step-by-step numerical implementation of MEX-AM in commonly available commercial software Ansys Fluent. The goal is to make the details of implementation openly accessible to the modelling community to further the studies beyond this point – rather than repeating similar studies.

2. Numerical method

This paper presents a model considering the motion of the nozzle by using a novel approach to meshing in

the context of modelling extrusion printing. By using the overset approach greater control of the refinement is provided by breaking up the computational domain into separate meshes and coupling the solutions of both grids. The method was developed in the CFD software ANSYS Fluent R22.1. The workflow of the method is outlined in Figure 1, showing an overview of the steps undertaken in the process.

2.1. Governing equations

The model presented within this paper considers the extrusion of a highly viscous medium, within the domain shown in Figure 2. The fluids modelled within the domain are considered incompressible due to the time scales and pressure changes. As such the densities of the air and extruded material are modelled as constants. As such, the pressure-based solver was selected in Ansys Fluent which is governed by the Navier-Stokes continuity equation and the momentum equation in the forms shown in Equations (1) and (2), respectively.

$$\nabla \cdot \mathbf{v} = 0 \quad (1)$$

$$\frac{\partial \mathbf{v}}{\partial t} + (\mathbf{v} \cdot \nabla) \mathbf{v} = -\frac{1}{\rho} \nabla p + \nabla \cdot \boldsymbol{\sigma} + \mathbf{g} \quad (2)$$

where \mathbf{v} is the velocity vector, t is time, ρ is the density, p is the pressure, $\boldsymbol{\sigma}$ is the deviatoric stress tensor, ∇ denotes the vector differential, and $\mathbf{g} = (0, -9.81, 0)$ is the gravitational acceleration vector. Neglecting elastic behaviour, the viscous deviatoric stress tensor becomes

$$\boldsymbol{\sigma} = 2\mu\mathbf{D}, \quad (3)$$

in which μ is the plastic viscosity, $\mathbf{D} = (\nabla\mathbf{v} + \nabla\mathbf{v}^T)/2$ is the deformation rate tensor, and T is the transpose notation.

Due to the high viscosity of the material of interest and the low velocities within the domain, viscous forces dominate the flow regime, and as such flow can

be considered laminar. This effected the nozzle geometry used throughout. The length of the nozzle needs only be great enough for developed flow to established. Given the dominance of viscous effects the required length is orders smaller than mm . The length used was 1.6 mm such that the nozzle model could be reused for less viscous fluid as well as allowing for the nozzle to be large enough in size such that the extruded fluid does not flow over the nozzle. The geometry was a 45° tapered nozzle with a face diameter of 0.8 mm and a nozzle diameter of 0.4 mm . To allow for the air and extruded medium to be modelled, the problem was approached as a two-phase flow of immiscible fluids. Using the volume-of-fluid (VOF) method [27], a primary phase (air) and a secondary phase (the extruded material) were defined and the governing equation for both fluids was solved together throughout the domain in a single momentum equation. The explicit finite-difference scheme was selected for the VOF temporal discretisation formulation. This scheme was selected due to its better interface tracking over the implicit scheme, as well as being less computationally expensive. The explicit scheme solves the VOF formulation using the finite difference forward Euler method. As such, the solution stability is time-dependent and a sufficiently small time-step must be used. The use of the implicit scheme, is still viable should the problem become stiff and not practical for the explicit formulation, though it is generally regarded as having poorer performance when the interface tracking is of concern.

A limitation of this approach is the stability relation to the ratio of viscosities between the phases. As the viscosity of the secondary phase must be sufficiently high to immobilise it, the ratio exceeds the ratio of stability in the Ansys Fluent solver (which is 1000) [28]. As such, the viscosity of the primary phase was increased to reduce this ratio to a stable value. The employment of the implicit scheme could likely negate this problem, however, the primary phase is the phase of least interest and it is a standard solution recommended by the Ansys Fluent user guide. Employing this approach, a viscosity sufficient to immobilise the secondary phase was only required, and as such a value of $2000\text{ Pa}\cdot\text{s}$ was assigned. This value fell in line with the order of values in [16,19,21]; a density of 1240 kg/m^3 was used based on the densities of the material in [29]. For the primary phase, the viscosity of air was increased by a multiple of 1000 to reduce the ratio of phases into stable levels, yielding a value of $0.01\text{ Pa}\cdot\text{s}$. Surface tension modelling was included, these effects would dominate only at very low velocities such as when at rest as the viscous forces during extrusion dominate. The method used by Ansys Fluent is the continuum surface force approach

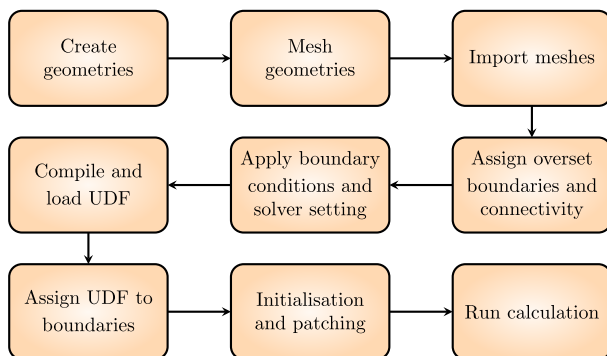


Figure 1. General workflow of the methods conducted in this study.

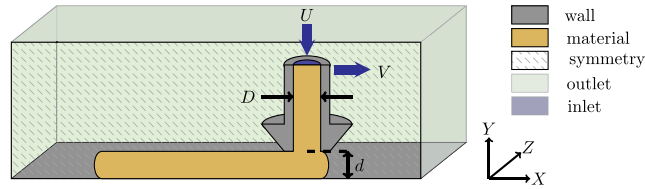


Figure 2. Computational domain of the MEX-AM process with associated boundary conditions as well as the process parameters (U is the volumetric velocity, V is the nozzle speed, D is the nozzle diameter, and d is the printing depth).

proposed by Brackbill et al. [30] where a surface force term is appended to the momentum equation. In the two-phase case, the equation takes the form of [28]

$$F_{vol} = \sigma_{12} \frac{\rho k_1 \nabla \alpha_1}{\frac{1}{2}(\rho_1 + \rho_2)} \quad (4)$$

where σ is the surface tension coefficient, ρ the density, k the curvature, $\nabla \alpha$ the local gradient of the interface, and the subscript 1, 2 indicating the two phases.

The surface tension between air and the material was set to 0.04 kg/s^2 [16]. It should be noted that the use of surface tension modelling with the selected meshing approach is a beta feature in Ansys Fluent and may lead to instability. The SIMPLEC pressure-velocity scheme, second-order upwind momentum discretisation, and modified body force weighted pressure discretisation were used for all simulation cases.

2.2. Overset meshing

To implement mesh motion the overset approach was used. The overset method is a grid-embedding method developed initially by [31] under the name ‘Chimera’ and expanded on by [32] – allowing for the use of unstructured 3D meshes. The approach is well-established and allows the embedding of multiple meshes within a singular computational domain. This greatly simplifies grid generation with the relative motion of boundaries while also allowing for body-conforming and unstructured meshes on the component sections of the domain. The performance of such an approach is noted to be largely dependent on the interpolation method between grids, particularly in high-flow gradient regions. Likewise, spatial discretisation mismatch and poor overlap between grid-boundaries can lead to degradation in the method’s performance [31]. As such, care must be taken to create meshes which account for these performance effectors. The main advantage of the application of this method is allowing for a dynamic mesh without the need for re-meshing or smoothing.

In the implementation within this paper, two meshes – the background and the component (nozzle) mesh – are connected by an overset interface which defines the region where cell data is interpolated between the

overlapping regions. To establish connectivity between the background and component mesh an hole-cutting process is performed by Ansys Fluent. This process identifies elements inside the wall boundaries and outside the computational domain as dead-cells. Overlap minimisation can then be employed to reduce the number of elements overlapping between the background and component meshes by identifying redundant elements and marking those as dead. Cell size or boundary distance-based donor priority methods can be employed. Once connectivity has been established, the method initiates the donor search process, identifying receptor cells and their associated donor cells. These receptors receive values based on their connectivity to neighbouring donor cells. Receptor cell values are generated by interpolating data from the donors which are interpolated through Equation (5)

$$\phi^h = \sum_{i=0}^N w^i \phi^i, \quad (5)$$

where ϕ is the solution variable N is the number of donors and w is the interpolation weights. The least-square weighting method is more accurate than the inverse distance method and as such was employed throughout. In the donor search protocol, a minimum of a four-cell overlap between the two meshes is required such that the solver can identify donor and receptor cells. If connectivity is not able to be established and a receptor cannot find a valid donor it will become an orphan cell. While Ansys Fluent can resolve this with a ‘best guess’ approach, it should be avoided as it is not rigorous and can lead to the divergence of the solution. Similarly, size mismatch between donor and receptor, that is mismatched between background and component mesh, can cause orphaning. Matching background and component element sizes within the overlap region will reduce the error associated with interpolation of data across from a donor to a receptor cell and mitigate orphaning – see Figure 3 for more clarification.

A symmetry condition was chosen to reduce domain size and computational cost. A structured hexahedron grid was used for the background mesh, refined around the expected region of flow – see Figure 4(a).

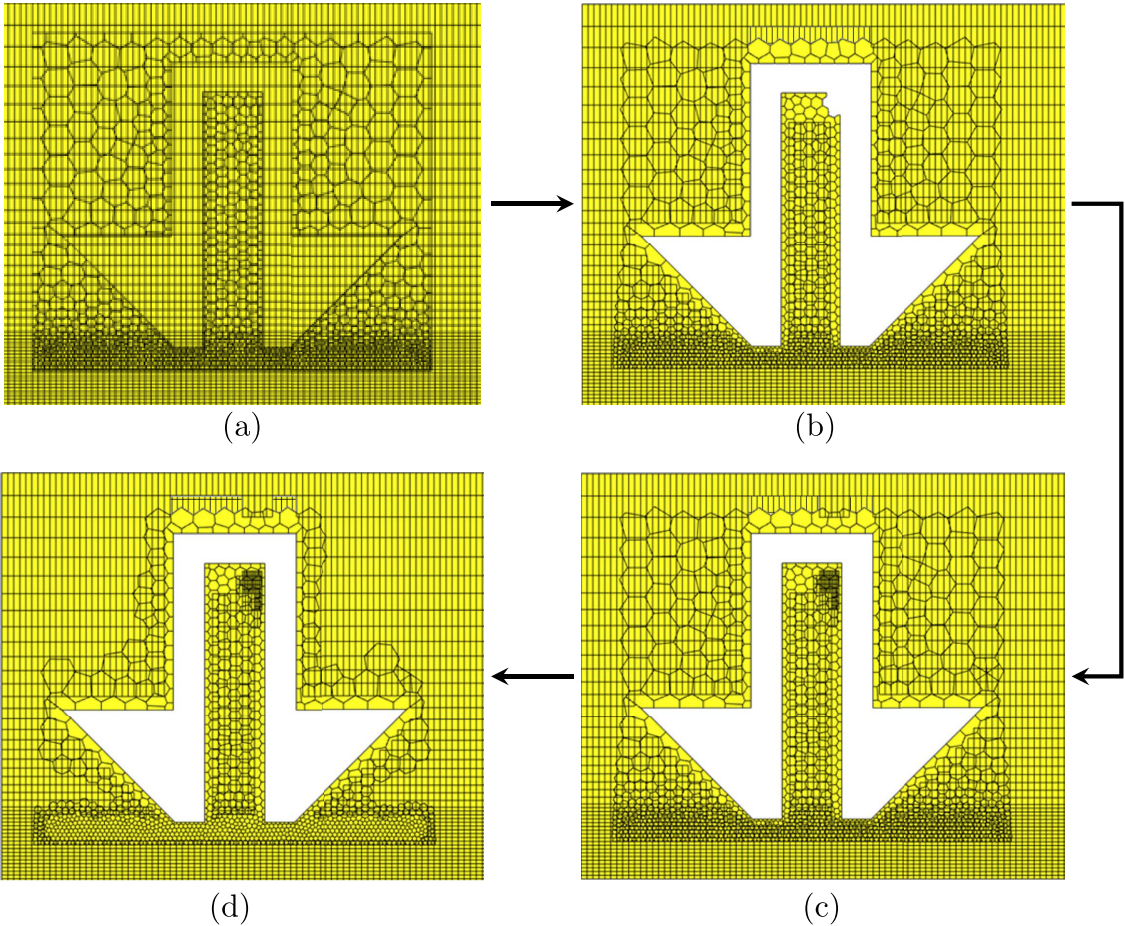


Figure 3. Example of overset meshing and adaptation for creating optimum mesh topologies including (a) overset meshing, (b) overset hole cutting, (c) overset adaptation, and (d) overset minimisation.

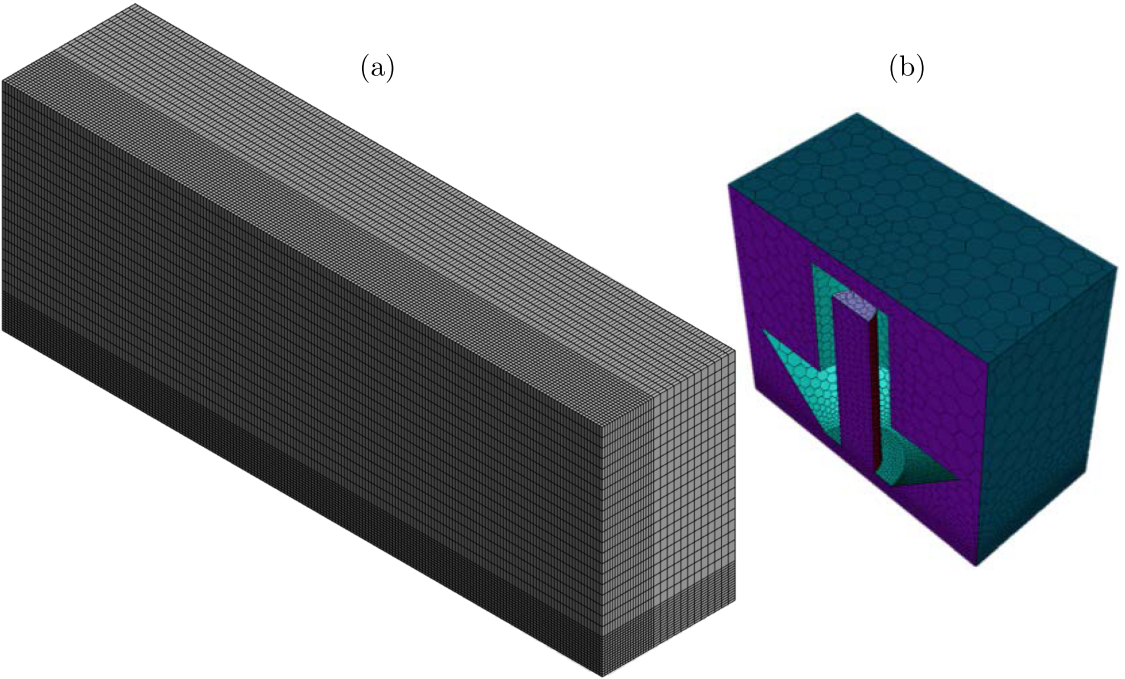


Figure 4. Single layer mesh for validation study, (a) the background mesh, and (b) the nozzle geometry mesh.

A poly-hexcore hybrid mesh was chosen for the nozzle geometry – see Figure 4(b) – and boundary sections were named for overset meshing.

Overset adaptive meshing was employed to refine the mesh only in regions where cell orphaning occurred. This method identifies cell orphaning and subdivides the meshes locally. The process is deterministic leading to predictable results which can be tested before running the solver to ensure satisfactory results during the adaptive process. After the timestep, the refinement is coarsened to reduce the global element count and not lead to runaway element numbers. The process is addressed more comprehensively in Section 6.7.5. of the Ansys User Guide [28].

2.3. Nozzle motion

To define the motion profile with which the nozzle moves, a user-defined function (UDF) was used. This UDF is created in the C/C++ programming language in an IDE of choice and then the source code file compiled within Fluent using the built-in compiler. This builds a library with this additional functionality, which is then loaded into the Fluent solver. Motion is achieved by assigning velocities to the boundaries of the nozzle component mesh for a set flow time duration. Using the function 'CG_MOTION' linear velocities and angular velocities could be applied by assigning values to the 'vel []' and 'omega []' arrays respectively. To assign this UDF to the component mesh boundaries, the dynamic mesh tab is used within Fluent. UDF source files for single-layer cases, including nozzle motion, are given in Appendix 1.

2.4. Initialisation and patching

The standard method of initialisation was conducted with the domain initialised with a velocity of 0.00 m/s and the domain as entirely primary phase (air). After which, the inside of the nozzle was patched with a secondary phase fraction value of 1, such that the interior of the nozzle was all the secondary phase (polymer). The velocity was also patched within this region to the inlet velocity of 0.02 m/s in the ($-y$) direction. This was implemented to improve the stability of the simulation.

2.5. Calculation settings

For the solver settings, a VOF-adaptive time step was used, with the Courant–Friedrichs–Lewy (CFL) number of 1 set as the control for the timestep. This allowed the solver to adapt the time step to ensure the CFL number was below 1 and ensure the stability of the

simulation. An initial time step of 0.001 s was used as the nozzle begins stationary so is less sensitive allowing a large time step to be used. However, once the motion had started the solver reduced the time step. A total number of 30 iterations per time step were used. This resulted in run times of between 9–18 hours per simulation on a 12-core Ryzen 9 3900 and 16 GB of RAM. The solver was parallelised to use 12 physical cores and 4 simultaneously multi-threaded cores. The double precision solver was used.

2.6. Post-processing

To extract the shape of the extruded material, an iso-surface of the secondary-phase fraction was taken. The value of the iso-surface was 0.5, representing the definite interface between the air and the extruded material. The iso-surface was taken at a plane that cut the extruded strand and exported in CSV format to then be imported into MATLAB for post-processing. However, Ansys Fluent exports the data by node number and as a result the data was a cloud of unordered points with no connectivity information. As such, the points required ordering such that the cross-section could be recreated. To do this an algorithm was used to connect randomly ordered points into a minimal nearest neighbour in a closed contour [33]. Additionally, as symmetry had been used for the domain, the node data had to be mirrored along the symmetry plane within MATLAB to then get a full contour of the cross-section.

3. Results and discussions

3.1. Mesh independence

A mesh independence study was conducted for a simple in-plane case of simulating one stand. The lessons learnt from this study were used in other cases for the mesh design. To compare the three meshes, the grid convergence index (GCI) [34] was used as

$$GCI = \frac{F_s |e|}{(r^p - 1)} \quad (6)$$

where p is the order of the simulation, F_s is the safety factor (3 was selected to be robust), e is the error between grids, and r is the refinement ratio (1.3 was used in this study). A refinement ratio of 1.3 was used as recommended by [35], however, for the component mesh (the nozzle region with unstructured mesh) the effective grid refinement ratio was used as in Equation (7). Here, N_1 and N_2 are the total number of elements and D is the dimension of the problem – 2

or 3 for 2D or 3D problems, respectively. The formal order of the simulation is different from the observed order, therefore, Roache [34] advocated the use of the effective order given in Equation (8), which considers the solution for the three meshes f_1 , f_2 and f_3 .

$$r_{eff} = \left(\frac{N_2}{N_1} \right)^{\frac{1}{p}} \quad (7)$$

$$p_{eff} = \frac{\ln \left(\frac{f_3 - f_2}{f_2 - f_1} \right)}{\ln(r)} \quad (8)$$

Three meshes were generated for both the background and the component (nozzle) meshes; a fine, coarse and medium mesh with increasing element counts. The elements of the meshes are shown in Table 1. To compare the cross-sections, a position 1 mm upstream from the initial nozzle location was selected, this position is far enough away from the nozzle for the strand shape to be fully developed but far enough away from the initial position where over-deposition occurs at the start.

The results of the study are shown in Figure 5. It can be seen that the medium and fine meshes (meshes 2 and 3, respectively) yield near identical cross-sections. The aspect ratio was examined as it considers the width and height of the cross-section. The aspect ratios were 0.860, 0.868, 0.875 for meshes 1, 2 and 3, respectively. The GCI yield values of 0.0381 and 0.0359. Therefore, as the morphology on meshes 2 and 3 are very similar, the use of this refinement cell size (0.025 mm) was appropriate.

3.2. Validation

To validate the model a parameterisation study was conducted on a single 5 mm strand. Eight different combinations of V/U and d/D were conducted and compared to experimental data from [23] and numerical data in [19]. The summary of the values used for each case in the validation study is presented in Table 2.

The numerical results in [19] used a different nozzle shape than that which was used in this model and the experiments in [23]. However, the inner diameters are the same, representing the common nozzle diameter used in FFF [36]. The results in [19] used the moving

Table 1. The number of elements used for the background and component (nozzle) domain for mesh independence analysis.

Mesh	Description	Background Elements	Component Elements	Size [mm]
1	Coarse	75946	17312	0.030
2	Medium	178126	40271	0.025
3	Fine	388720	79977	0.020

Note: Size refers the the refinement element size.

bed condition and provided a comparison of the methods. In [23] three repeats were conducted, for this validation the average result of the three repeats was considered. Two meshes were required for this study, offering an advantage over the method in [19] which required a unique mesh for each d/D . In this study the component mesh in this model just required its initial position changing. The elements of the component mesh at the exit of the nozzle were the same within the refined region of the background mesh. The results of the study are shown in Figure 6. The figure shows the cross-sections of the deposited strand from the numerical simulations in the foreground with the scaled image of the experimental results in [23] behind. The position of the nozzle relative to the bed is also shown.

The numerical results generally align with the experiments, despite the simplified model omitting thermal effects and material properties, extending the model to include these phenomena – such non-isothermal models and surface tension forces – would likely lead to a better agreement. The model appears to have less side flow which could be due to the location difference that [23] took the cross-sections. The locations closer to the nozzle will be wider, however, this location is not reported in the paper. Experimentally the material rises in the centre which is not captured in the simulation cross-sections shown in Figure 6. This could potentially be a material property or related to material adhesion to the nozzle, pulling up the centre of the nozzle. Indeed, cross-sections closer to the nozzle in the simulation do exhibit this behaviour, but it is not carried throughout the strand. In Figure 6 for parameters $d/D = 0.6$, $U/V = 0.5$ it can be seen there is rounding of the edges of the strand. The reason for this could be the relatively viscous air entrainment, or spurious currents, which are non-physical vortices occurring at the interface of the phases. These tend to occur in VOF simulations with high viscosity ratios [37]. If this is the case,

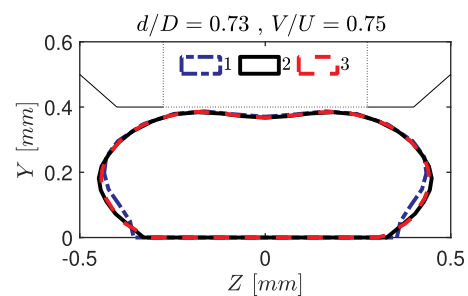


Figure 5. Cross-sections of the strands for the three meshes, fine, medium and coarse given in Table 1. Mesh 2 and 3 yield nearly identical results.

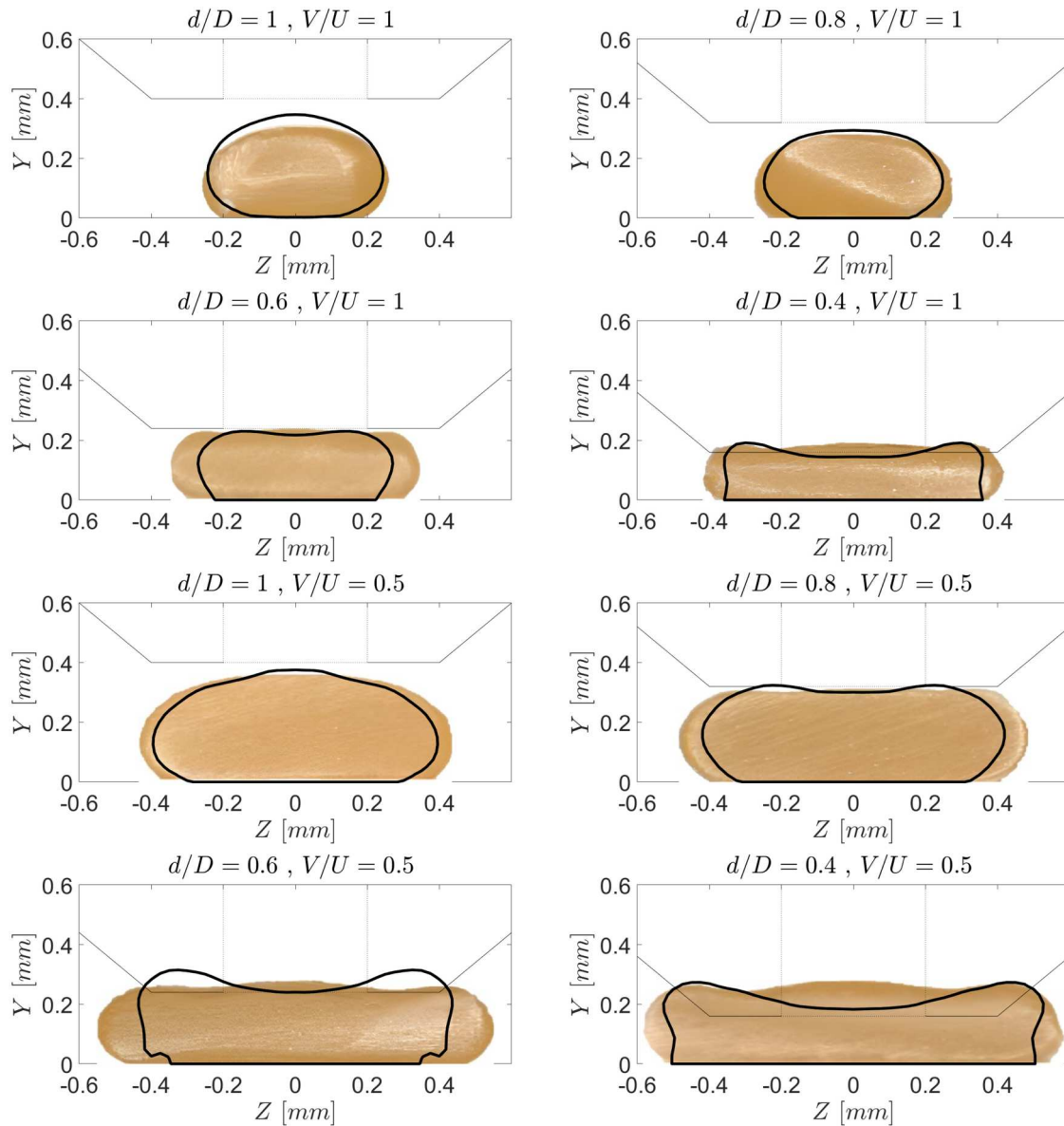
Table 2. Summary of values used in the cases of the validation study.

Variable	Symbol	Value	Unit
Nozzle diameter	D	0.40	mm
Print height	d	0.16, 0.24, 0.32, 0.40	mm
Nozzle velocity	V	10, 20	mm/s
Volumetric velocity	U	20	mm/s

then using the combined VOF and Level-Set method (CLSVOF) model would likely solve this issue [38].

The results, moreover, were compared with the experimental data and the numerical results of [19] along with the idealised shape of an ellipse which is typically used in analytical analysis (see Figure 7). It can be seen that for the $U/V = 1$ the thickness of the results closely follows that of [19] but begins to diverge more for $U/V = 0.5$.

This is due to the centre rising of the strands which has been addressed before. The strand width follows the expected trend but is shifted down from the trends in [19,23] which is likely due to the different cross-section positions and material side-swelling. The nozzle geometry in [19] is a flat-faced nozzle and not a tapered nozzle, which could be the reason their results match the experimental data better. Because there is more side swell due to differing mass conservation without the rise around the tapered nozzle. Indeed this is noted in the paper that the nozzle geometry will affect this side swell. It is generally expected for there to be differences between the numerical method and experimental data. This is mainly because the numerical model introduces a number of errors such as truncation error,

**Figure 6.** Morphology of the experimental strands in [23] with the simulation results indicated as bold lines. The nozzle position is indicated by the thin lines.

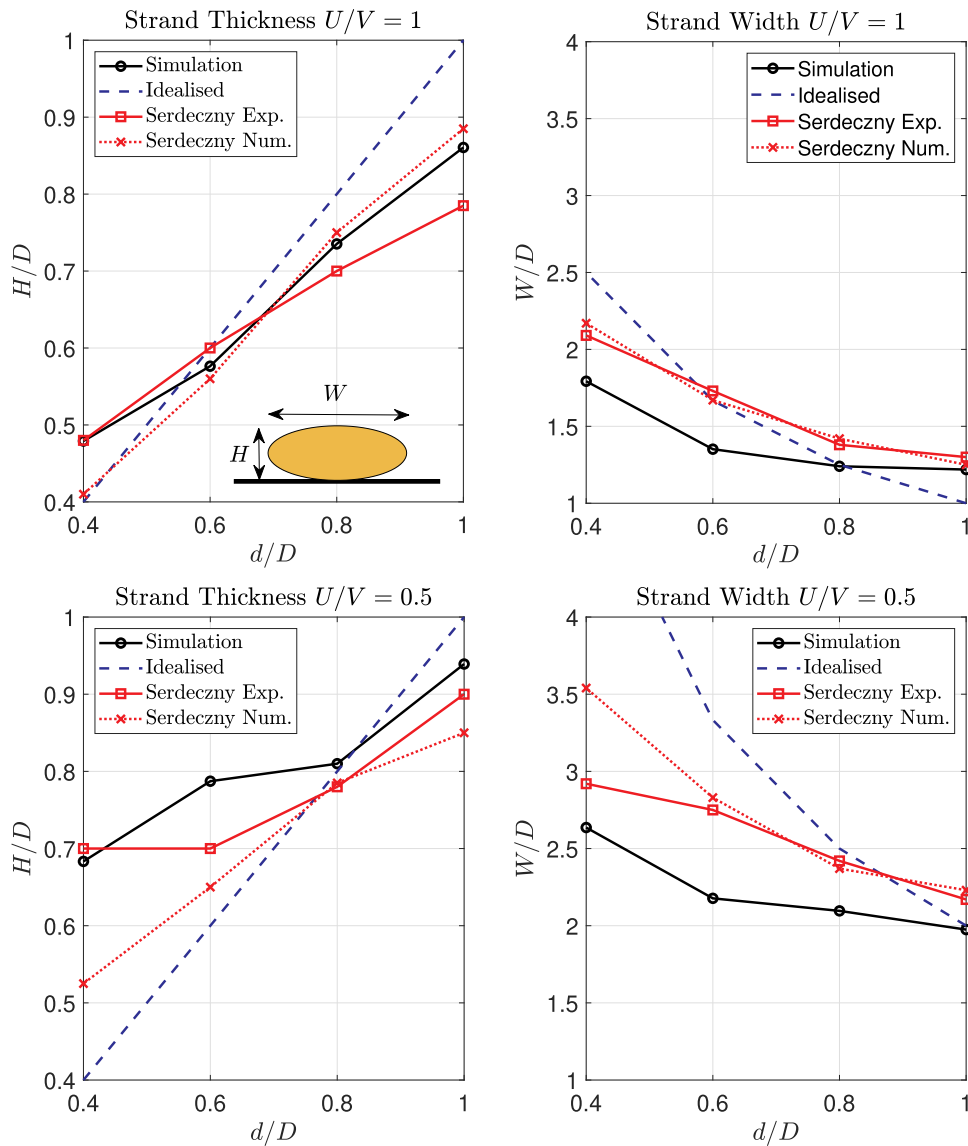


Figure 7. Comparison of the simulated results of the non-dimensionalised thickness and width of the strands against the experimental and numerical results in [23].

discretisation error, round-off error and convergence error. It is important to note that all these errors are somewhat interrelated. Since the mesh sensitivity analysis has been conducted, and higher-order schemes are used with double precision, we believe that solver (relaxation factors) setting in Ansys could be the main source of error.

3.3. Out-of-plane motion

To demonstrate the model's capability in allowing out-of-plane motion, two case studies were conducted. An initial case demonstrating a multi-layer print and an inclined print bed to demonstrate nozzle rotation. The qualitative result of the three-layer demonstration can be seen in Figure 8(a). The nozzle can move out of

plane and back to its original location depositing two and three layers of extruded material. The Newtonian model used is not completely satisfactory for capturing the expected result from a multi-layer deposition. As it can be seen in Figure 8(b) when the upper layers are deposited the first layer cross-section is reduced from the height of 0.38 mm to 0.31 mm and 0.27 mm for two-layer and three-layer cases, respectively. This is due to compaction by the weight of the secondary layers. Over multiple layers, this result may compound leading to the complete flattening of the bottom layer. The reason for this is suspected to be the materials' viscosity model. The bottom and top layers have the same viscosity, so the upper layer is readily able to displace the bottom layer. In the deposition of a viscous Newtonian material, this may be correct but for non-Newtonian

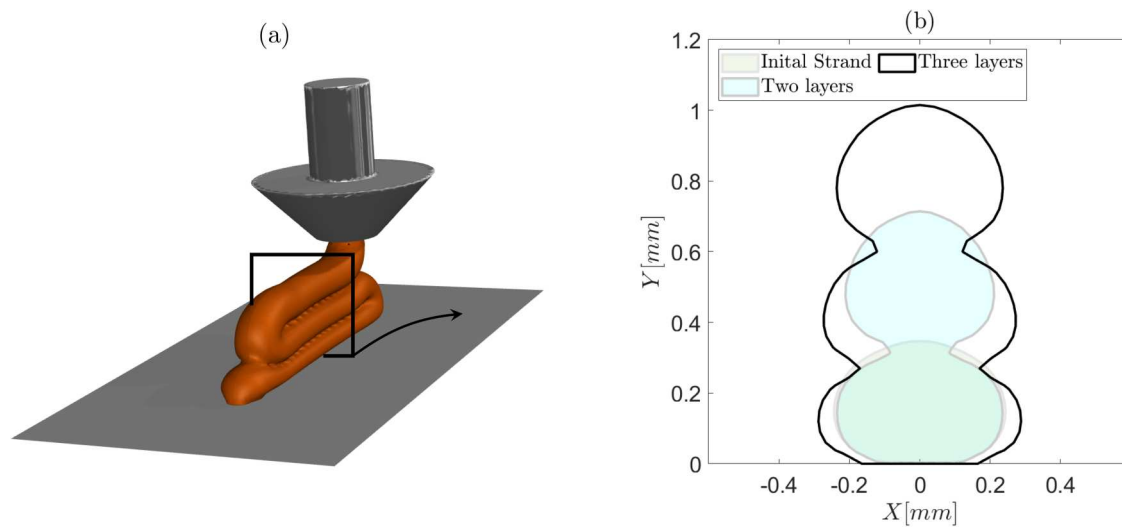


Figure 8. Two layer MEX-AM, (a) qualitative view of the three deposited strands, and (b) cross-section of deposited layers.

and viscoelastic materials the effects of strain and temperature need to be included. UDF source file for the two-layer case study is presented in Appendix 2.

For the ramped case, the nozzle was prescribed a motion to follow the wall boundary, maintaining a distance of 0.4 mm from the bed. For the non-angled case, the 0.4 mm distance was maintained from the inner edge of the nozzle furthest away from the bed. For the angled case, the nozzle was rotated to be always parallel to the bed (printing path). The effect on the morphology of the strand was investigated. The methodology remained the same as with the other cases, however a different UDF and mesh were required to allow for the motion path. The UDF calculated the angle of rotation between the flat and angled portion of the bed and by assigning a rotational velocity of 15 rad/s to the nozzle via the ' ω ' array – modifying the dynamic components a rotational velocity – the nozzle could be rotated. A comparison between the angled and non-angled nozzle was conducted to demonstrate an avenue of research which has not been carried out before. UDF source file for the ramped bed case study is given in Appendix 3.

The qualitative result of the non-angled nozzle simulation is shown in Figure 9(a). It can be seen that the nozzle moves up the ramp and deposits material along the inclined bed. The comparison between the height of the strand for the angled and non-angled cases is shown in Figure 9(b). It is seen that the height difference between the strands is almost negligible, but with a region of under deposition occurring at 6 mm on the case where the nozzle does not angle itself, the two strand areas of the side profile have a 0.839% difference by area so yield negligible different side profiles.

In Figure 10 it can be seen that while not angling the nozzle does not affect the strands' height, it does influence the strands' width. It is worth noting that for extracting strand shapes along the ramped bed, the cross sections were always taken normally to the print bed, and the cross sections at locations 3 mm and 5 mm lie on the ramp. Without rotating (non-angled case) the nozzle, the strand's width is increased in the ramp compared to the angled case. This is due to the nozzle having the front edge much closer to the bed, and the rear leading to over deposition and more side flow of the material. At the 5 mm location, the top of the strand rises to form a ridge. This ridge is present on both strands but is much more evident on the angled case. This might be a result of the model or motion plan, drawing material up, or possible wicking effect at the rear of the nozzle. There is a difference in strand morphology at positions 1 mm and 7 mm despite both these locations being flat portions of the bed. This difference is due to the locations where the cross-sections are taken, with the strands being more and less developed respectively. At the 7 mm location, the cut has a closer proximity to the nozzle and as such is influenced by the swell and over-deposition around the nozzle, whereas the cut at 1 mm has developed into the final cross-section as the nozzle moved away from this location drawing with it the over deposited material. This same behaviour is seen for both the angled and non-angled cases which yield identical results at these positions.

From this brief study it can be assumed that by angling the nozzle, the strand maintains a more uniform rounded morphology, and by maintaining the nozzle such that it is not normal there is greater side flow. The approach used may depend on the

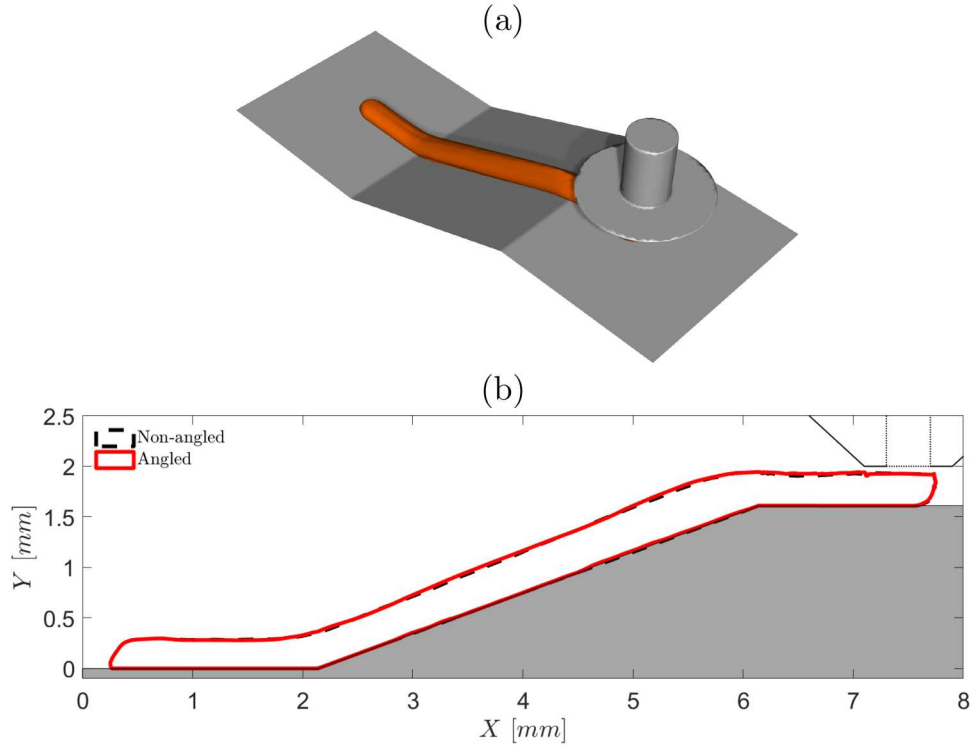


Figure 9. Isosurface result of (a) the non-angled nozzle motion, (b) view of the two strands (the angled and non-angled) on a ramped bed.

application, the latter may provide fewer inter-layer voids due to this increased side flow but leads to greater dimensional instability and poorer surface finish. The former will provide a thinner strand which may give a better surface finish. These cases have shown the ability of the presented model for the nozzle to rotate and move out of plane, demonstrating the method's capability for other forms of movement and motion planning.

3.4. Extending the material model

The model was extended to include non-isothermal and non-Newtonian flows to demonstrate applications where the Newtonian and isothermal models are not sufficient. The implementation of the non-isothermal model required enabling the energy conservation equation and applying the appropriate boundary conditions as well as initialising the domain to the correct temperatures. The energy conservation equation is given by

$$\frac{\partial(\rho E)}{\partial t} + \nabla \cdot (\rho \mathbf{v} E - \mathbf{v} \cdot \mathbf{q}) = \nabla \cdot (\boldsymbol{\tau} \cdot \mathbf{v}) + \nabla \cdot (\mathbf{v} \cdot \mathbf{p}) + \rho \mathbf{g} \cdot \mathbf{v} + S_E \quad (9)$$

where ρ is the density of the fluid, E is the internal energy per unit mass, \mathbf{v} is the velocity vector, \mathbf{q} is the heat flux

vector, $\boldsymbol{\tau}$ is the stress tensor, p the pressure, \mathbf{g} the gravitational acceleration vector, and S_E the source term for internal energy. For the non-Newtonian model, the well-known Cross-William-Landel-Ferry (Cross-WLF) model was used. This is an extension of the Cross model that includes the temperature, strain rate and pressure dependency of a thermoplastic material using a seven-constant model for the zero shear viscosity, μ_0 . The dynamic viscosity, μ , of the material, is given by

$$\mu(\dot{\gamma}, T, p) = \frac{\mu_0(T, p)}{1 + \left(\frac{\mu_0(T, p) \cdot \dot{\gamma}}{\tau^*}\right)^{1-n}}, \quad (10)$$

where $\dot{\gamma}$ is the shear rate, T is the temperature, p is the pressure, τ^* is the critical stress level at the transition to shear thinning, and n is the power-law index in the high shear rate regime. The zero-shear viscosity is

$$\mu_0 = D_1 \exp \left[-\frac{A_1(T - T_g)}{A_2 + (T - T_g)} \right] \quad (11)$$

in which the glass transition temperature is $T_g = D_2 + D_3 p$, D_2 being the value of T_g at atmospheric pressure and D_3 is related to the material compressibility. The values A_1, A_2, D_1, D_2 and D_3 are data-fitted constants, and in this paper, the parameters are summarised in Table 3. With such a model, at low shear rates and temperatures, the viscosity can become significantly more orders above

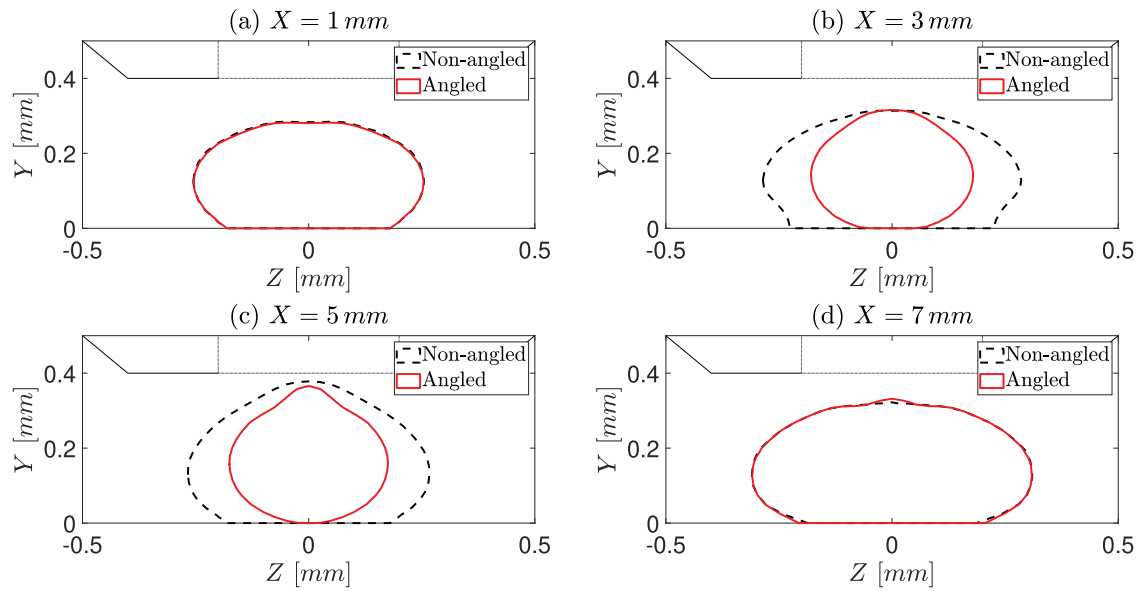


Figure 10. Cross-sections at X locations of (a) 1 mm, (b) 3 mm, (c) 5 mm, and (d) 7 mm along the strands. Positions relative to the domain can be seen in Figure 9(b).

that of the primary phase to cause instability. Hence, the viscosity was limited to $5000 \text{ Pa}\cdot\text{s}$ as the viscosity only required to be high enough to immobilise the fluid. Without capping the viscosity, it may require many more iterations to converge the solution, requiring computational resources that would not be practical for demonstrating the implementation. For the material to flow, the secondary phase must be above the glass transition temperature, as such the model was initialised with the patched secondary phase at 473.15 K inside the nozzle, with the same applied to the inlet. The air was 293.15 K and the internal walls of the nozzle were given a temperature of 473.15 K as well.

For the UDF the 'DEFINE_PROPERTY' was used. Macros available in the UDF library were used to retrieve the shear rate and temperature within a cell – see Appendix 4. The material used in [29] exhibited no pressure-related effects, which was reflected in the UDF. Even with an implicit solver the viscosity ratio remained high enough to cause instability in the solver which could not be addressed with relaxation factors (as this would violate continuity). As such, like in the general methodology, the

viscosity of air was raised to those values. The same meshes that were used for the single-layer case were used, with $d/D = 1.0$. The wall boundary conditions were modelled as the default aluminium material in Fluent. As the results in Figure 11 show, the model can be extended to include a non-isothermal and non-Newtonian model and successfully print a single strand.

In Figure 11 it can be seen that within the inside of the nozzle, the viscosity is significantly lower than that of the upstream deposited material. As the material is extruded through the nozzle, it adheres to the nozzle walls increasing the strain rate locally to values of 1080 s^{-1} , thinning the material. At the centre of the nozzle, the shear is much lower and about 150 s^{-1} which results in an increased viscosity. Notably, the viscosity at the walls is around $250 \text{ Pa}\cdot\text{s}$ and $3700 \text{ Pa}\cdot\text{s}$ at the centre of the nozzle. Upstream at the cooled portion, the viscosity rises to $5000 \text{ Pa}\cdot\text{s}$ due to the cooling of the material and low strain rates. If the viscosity modelled was not capped at $5000 \text{ Pa}\cdot\text{s}$ it is expected that the viscosity would be much greater upstream. This is due to the transition of the material to a much higher viscosity once the temperature drops below its T_g . The removal of this cap would likely yield more iterations to achieve convergence. The viscosity is low again under the nozzle where the extruded material expands radially outwards after exiting the nozzle, increasing the strain of the melt and lowering the viscosity to $2470 \text{ Pa}\cdot\text{s}$. Shear-thinning of the material at the exit of the nozzle will allow for successive layers to be printed atop each other without the squashing effect presented earlier – see Figure 8(a). Another effect of the no-slip condition on the walls is

Table 3. Cross-WLF viscosity model parameters [29].

Parameters	Value	Unit
A_1	20.194	–
A_2	51.6	K
D_1	$3.31719\text{E}+9$	$\text{Pa}\cdot\text{s}$
D_2	373.15	K
D_3	0	K/Pa
T_g	373.15	K
n	0.25	–
τ^*	$1.00861\text{E}+5$	Pa

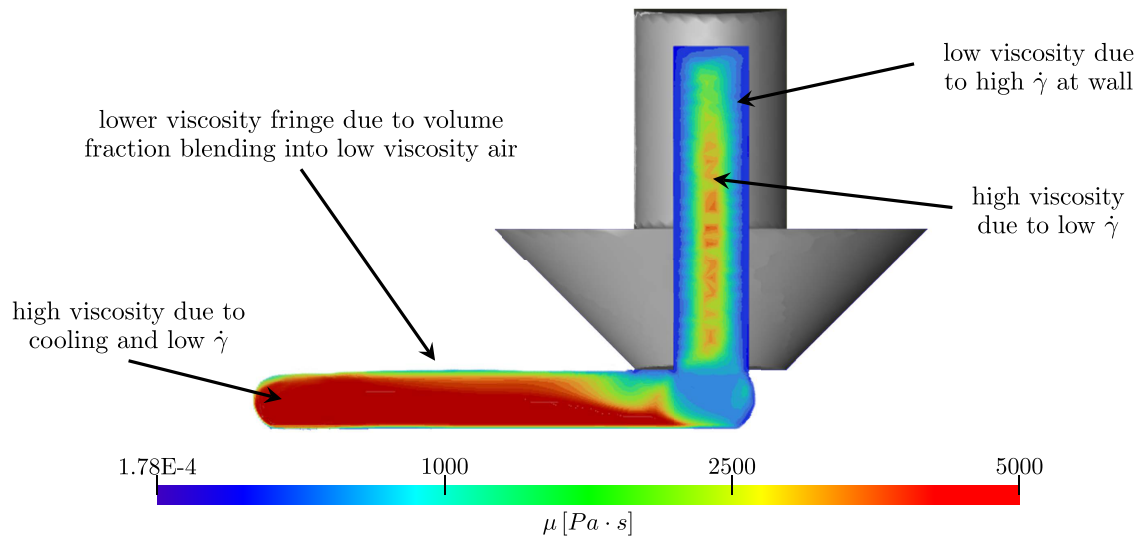


Figure 11. Viscosity variation during MEX-AM of single strand using Cross-WLF model.

the retardation of the flow near the walls and the acceleration of the flow at the core of the nozzle. The core is accelerated to 29.4 mm/s greater than even the inlet velocity to maintain mass conservation – as a result of the slow flow at the nozzle walls. The effect of gravity is expected to be minor in the extrusion process due to the small length scales. The cooling pattern of the deposited strand can be seen in Figure 12. At the bottom of the strand, furthest away from the nozzle the material has cooled to 374 K increasing moving towards the nozzle to 473 K.

The application of these models demonstrates the versatility of the method as it can readily be extended to improve the twinning of the process with reality. This broadens the applications of the proposed model to cases where shear-thinning effects are necessary, such

as for the printing of ceramics. The rheology of the ceramic often limits its use as the pressures required to extrude the material would lead to sputtering. Likewise, with thermoplastics, the mechanical strength of parts is dependent on the bonding and void area, and with this proposed method the moving nozzle can allow for investigations into the printing of multiple layers and how the re-heating affects the bounding process.

4. Concluding remarks

The significance of this paper has been to present a method which allows for numerical simulation of MEX-AM with out-of-plane motion. The use of overset meshing and UDFs has proved an effective method of

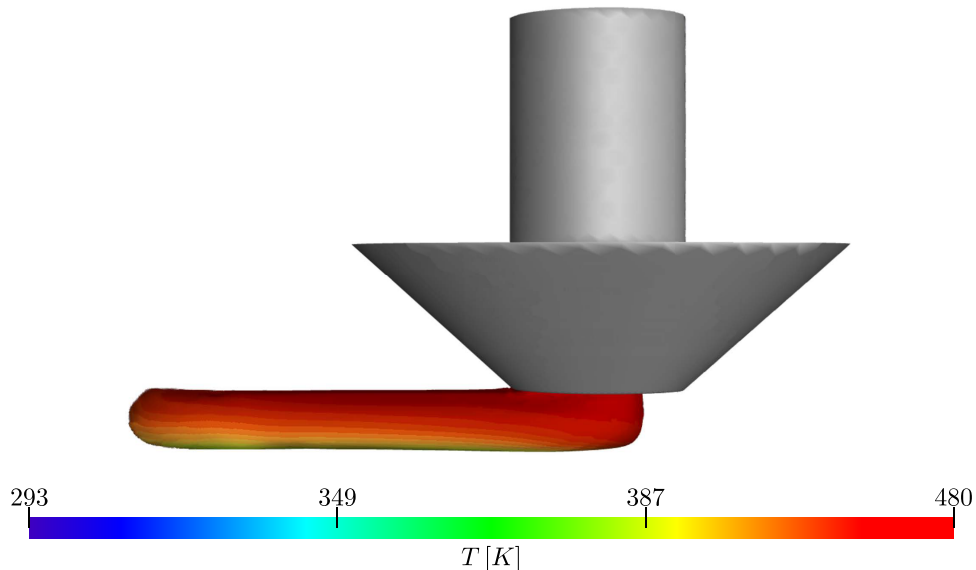


Figure 12. Contours of temperature during MEX-AM of single strand using Cross-WLF model.

implementing the nozzle motion. This method allows the near wall refinement to be explicitly defined, which was not possible in the IB method due to this not using body-fitted meshing techniques. The computational cost was not significant enough to be viewed as a limitation, but rather an area for refinement. In a general sense, this approach makes the mesh design less restrictive. The interpolation from the coupling of the grid did not appear to create any non-physical results. It was noticed that the residual behaviour converged well at each time step with consistent periodicity during motion. This indicates at each time step there was stability and the solution monitors were not being greatly influenced by the interpolation. It is likely that the ensuring elements overlapped well between grids minimised any interpolation issues.

Using this method, it was shown that incline beds and the printing of at least two layers are possible. While it is likely more layers could be extruded this was not explored simply due to computational cost. The more layers, the larger the domain and the greater the refinement needed, demonstrating the deposition of two layers acts as a framework for increasing the simulation of more layers. It demonstrated that by angling the nozzle to be parallel with the bed there is less side flow and as a result, the strand is more rounded and less thin. It was further shown that the model is robust enough to have its functionality expanded to include the non-isothermal model as well as non-Newtonian material flow. This is advantageous as it will allow the approach to be used for many different extrusion processes where physics varies for these particular cases.

The methodology in this paper may be used in conjunction with other models to numerically explore scenarios that previous models could not address. Further exploring innovative print bed configurations, such as inclined or gaped beds could provide printing strategies that enhance the versatility of MEX-AM by conducting parameter studies required for such scenarios. As evidenced in this project, multi-layer prints are feasible, and by expanding the material model, it is possible to account for the heat effects in multi-layer FFF simulations. This expansion opens doors for studying void density in multi-layer structures, devising strategies to minimise these voids and thereby enhancing the mechanical strength of the printed object.

Acknowledgments

For the purpose of open access, the authors applied a Creative Commons Attribution (CC BY) license to any Author Accepted Manuscript version arising from this submission.

Disclosure statement

No potential conflict of interest was reported by the author(s).

Funding

The authors would like to acknowledge the support from UK Research and Innovation Strength In Places Fund (project 84646) led by Professor Robert Richardson (PI).

CRedit authorship contribution statement

Max Galloway: Conceptualization, Methodology, Investigation, Formal analysis, Writing – original draft, Writing – review & editing. **Sung Hin Lam:** Methodology, Writing – review & editing. **Hoda Amel:** Writing – review & editing. **Robert Richardson:** Writing – review & editing, Supervision. **Robert Kay:** Writing – review & editing, Supervision. **Masoud Jabbari:** Conceptualization, Formal analysis, Writing – review & editing, Supervision.

Data availability statement

The data that support the findings of this study are available from the corresponding author upon reasonable request.

ORCID

Robert Richardson  <http://orcid.org/0000-0002-6232-1323>

Robert Kay  <http://orcid.org/0000-0002-2283-3789>

Masoud Jabbari  <http://orcid.org/0000-0003-3615-969X>

References

- [1] Esfahani RN, Shuttleworth MP, Doychinov V, et al. Light based synthesis of metallic nanoparticles on surface-modified 3d printed substrates for high performance electronic systems. *Addit Manuf.* 2020;34:101367.
- [2] Zhuo P, Li S, Ashcroft IA, et al. Material extrusion additive manufacturing of continuous fibre reinforced polymer matrix composites: a review and outlook. *Compos B Eng.* 2021;224:109143. doi: 10.1016/j.compositesb.2021.109143
- [3] Hadian A, Fricke M, Liersch A, et al. Material extrusion additive manufacturing of zirconia parts using powder injection molding feedstock compositions. *Addit Manuf.* 2022;57:102966.
- [4] Joshi SC, Sheikh AA. 3d printing in aerospace and its long-term sustainability. *Virtual Phys Prototyp.* 2015;10(4):175–185. doi: 10.1080/17452759.2015.1111519
- [5] Turner BN, Gold SA. A review of melt extrusion additive manufacturing processes: II. Materials, dimensional accuracy, and surface roughness. *Rapid Prototyp J.* 2015;21(3):250–261. doi: 10.1108/RPJ-02-2013-0017
- [6] Fonseca N, Thummalapalli SV, Jambhulkar S, et al. 3d printing-enabled design and manufacturing strategies

- for batteries: a review. *Small*. 2023;19(50):2302718. doi: [10.1002/smll.v19.50](https://doi.org/10.1002/smll.v19.50)
- [7] Chen G, Chen N, Wang Q. Fabrication and properties of poly (vinyl alcohol)/ β -tricalcium phosphate composite scaffolds via fused deposition modeling for bone tissue engineering. *Compos Sci Technol*. 2019;172:17–28. doi: [10.1016/j.compscitech.2019.01.004](https://doi.org/10.1016/j.compscitech.2019.01.004)
- [8] Braconnier DJ, Jensen RE, Peterson AM. Processing parameter correlations in material extrusion additive manufacturing. *Addit Manuf*. 2020;31:100924.
- [9] Yang L, Li S, Li Y, et al. Experimental investigations for optimizing the extrusion parameters on FDM PLA printed parts. *J Mater Eng Perform*. 2019;28:169–182. doi: [10.1007/s11665-018-3784-x](https://doi.org/10.1007/s11665-018-3784-x)
- [10] Turner BN, Strong R, Gold SA. A review of melt extrusion additive manufacturing processes: I. Process design and modeling. *Rapid Prototyp J*. 2014;20(3):192–204. doi: [10.1108/RPJ-01-2013-0012](https://doi.org/10.1108/RPJ-01-2013-0012)
- [11] Al Rashid A, Koç M. Experimental validation of numerical model for thermomechanical performance of material extrusion additive manufacturing process: effect of process parameters. *Polymers*. 2022;14(17):3482. doi: [10.3390/polym14173482](https://doi.org/10.3390/polym14173482)
- [12] Narei H, Jabbari M. 3d printing of polymer composites. In: *Applied complex flow: applications of complex flows and CFD*. Springer, 2023, pp. 107–123.
- [13] Comminal R, Serdeczny MP, Pedersen DB, et al. Numerical modeling of the strand deposition flow in extrusion-based additive manufacturing. *Addit Manuf*. 2018;20:68–76.
- [14] Narei H, Fatehifar M, Malt AH, et al. Numerical simulation of a core–shell polymer strand in material extrusion additive manufacturing. *Polymers*. 2021;13(3):476. doi: [10.3390/polym13030476](https://doi.org/10.3390/polym13030476)
- [15] Kim SK, Kazmer DO. Non-isothermal non-Newtonian three-dimensional flow simulation of fused filament fabrication. *Addit Manuf*. 2022;55:102833.
- [16] Xia H, Lu J, Dabiri S, et al. Fully resolved numerical simulations of fused deposition modeling. part I: fluid flow. *Rapid Prototyp J*. 2018;24(2):463–476. doi: [10.1108/RPJ-12-2016-0217](https://doi.org/10.1108/RPJ-12-2016-0217)
- [17] Comminal R, Serdeczny MP, Pedersen DB, et al. Motion planning and numerical simulation of material deposition at corners in extrusion additive manufacturing. *Addit Manuf*. 2019;29:100753.
- [18] Kovan V, Altan G, Topal ES. Effect of layer thickness and print orientation on strength of 3D printed and adhesively bonded single lap joints. *J Mech Sci Technol*. 2017;31:2197–2201. doi: [10.1007/s12206-017-0415-7](https://doi.org/10.1007/s12206-017-0415-7)
- [19] Serdeczny MP, Comminal R, Pedersen DB, et al. Numerical study of the impact of shear thinning behaviour on the strand deposition flow in the extrusion-based additive manufacturing. In: *18th International Conference of the European Society for Precision Engineering and Nanotechnology (euspen 18)*. The European Society for Precision Engineering and Nanotechnology, 2018, pp. 283–284.
- [20] Xu X, Wanglin Q, Wan D, et al. Numerical modelling of the viscoelastic polymer melt flow in material extrusion additive manufacturing. *Virtual Phys Prototyp*. 2024;19(1):e2300666. doi: [10.1080/17452759.2023.2300666](https://doi.org/10.1080/17452759.2023.2300666)
- [21] Serdeczny MP, Comminal R, Pedersen DB, et al. Numerical simulations of the mesostructure formation in material extrusion additive manufacturing. *Addit Manuf*. 2019;28:419–429.
- [22] Comminal R, da Silva WRL, Andersen TJ, et al. Modelling of 3D concrete printing based on computational fluid dynamics. *Cem Concr Res*. 2020;138:106256. doi: [10.1016/j.cemconres.2020.106256](https://doi.org/10.1016/j.cemconres.2020.106256)
- [23] Serdeczny MP, Comminal R, Pedersen DB, et al. Experimental validation of a numerical model for the strand shape in material extrusion additive manufacturing. *Addit Manuf*. 2018;24:145–153.
- [24] Xia H, Lu J, Tryggvason G. A numerical study of the effect of viscoelastic stresses in fused filament fabrication. *Comput Methods Appl Mech Eng*. 2019;346:242–259. doi: [10.1016/j.cma.2018.11.031](https://doi.org/10.1016/j.cma.2018.11.031)
- [25] Spangenberg J, da Silva WRL, Comminal R, et al. Numerical simulation of multi-layer 3D concrete printing. *RILEM Tech Lett*. 2021;6:119–123. doi: [10.21809/rilemtechlett.2021.142](https://doi.org/10.21809/rilemtechlett.2021.142)
- [26] Mollah MT, Comminal R, da Silva WRL, et al. Computational fluid dynamics modelling and experimental analysis of reinforcement bar integration in 3D concrete printing. *Cem Concr Res*. 2023;173:107263. doi: [10.1016/j.cemconres.2023.107263](https://doi.org/10.1016/j.cemconres.2023.107263)
- [27] Hirt CW, Nichols BD. Volume of fluid (vof) method for the dynamics of free boundaries. *J Comput Phys*. 1981;39(1):201–225. doi: [10.1016/0021-9991\(81\)90145-5](https://doi.org/10.1016/0021-9991(81)90145-5)
- [28] Ansys Incorporated: *Ansys Fluent User's Guide*, Jul. 2022.
- [29] Moldflow Plastic Labs: *Moldflow material testing report MAT2238-NatureWorks*, 2007.
- [30] Brackbill JU, Kothe DB, Zemach C. A continuum method for modeling surface tension. *J Comput Phys*. 1992;100(2):335–354. doi: [10.1016/0021-9991\(92\)90240-Y](https://doi.org/10.1016/0021-9991(92)90240-Y)
- [31] Steger JL, Dougherty FC, Benek JA. A chimera grid scheme, 1983.
- [32] Nakahashi K, Togashi F, Sharov D. Intergrid-boundary definition method for overset unstructured grid approach. *AIAA J*. 2000;38(11):2077–2084. doi: [10.2514/2.869](https://doi.org/10.2514/2.869)
- [33] Ursell T. Connect Randomly Ordered 2D Points into a Minimal Nearest-Neighbor Closed Contour. Available: <https://www.mathworks.com/matlabcentral/fileexchange/35488-connect-randomly-ordered-2d-points-into-a-minimal-nearest-neighbor-closed-contour>.
- [34] Roache PJ. Verification of codes and calculations. *AIAA J*. 1998;36(5):696–702. publisher: American Institute of Aeronautics and Astronautics. Available: <https://arc.aiaa.org/doi/10.2514/2.457>. doi: [10.2514/2.457](https://doi.org/10.2514/2.457)
- [35] Code Verification and Solution Verification. In: *Standard for Verification and Validation in Computational Fluid Dynamics and Heat Transfer.*, ser. American Society of Mechanical Engineers Guide. ASME, 2009, vol. 20, p. 7. Available: http://ftp.demec.ufpr.br/disciplinas/TM777/Apostila/Extrato_norma_ASME_VeV_20-2009.pdf.
- [36] Zhou Y, Lu H, Wang G, et al. Voxelization modelling based finite element simulation and process parameter optimization for fused filament fabrication. *Mater Des*. 2020;187:108409. doi: [10.1016/j.matdes.2019.108409](https://doi.org/10.1016/j.matdes.2019.108409)
- [37] Bohacek J. Surface tension model for high viscosity ratios implemented in vof model. In: *ILASS, 23rd annual conference on liquid atomization and spray systems*, 2010.
- [38] Solomenko Z, Spelt PD, Naraigh LO, et al. Mass conservation and reduction of parasitic interfacial waves in level-set methods for the numerical simulation of two-phase flows: A comparative study. *Int J Multiph Flow*. 2017;95:235–256. doi: [10.1016/j.ijmultiphaseflow.2017.06.004](https://doi.org/10.1016/j.ijmultiphaseflow.2017.06.004)

Appendix 1. Single layer UDF

```

include "udf.h"
static real velx=0.0;
static real vely=0.0;
DEFINE_CG_MOTION(box,dt,vel,omega,time,dttime)
{
    NV_S(vel, =, 0.0);
    NV_S(omega, =, 0.0);
    float move_time=0.018f; //hold nozzle still so flow can leave the nozzle and make contact with bed without nozzle moving
    float stop_time = 0.268f; // time when to stop moving nozzle
    if (time < move_time — time < stop_time)
        velx = 0;
    }
    else{
        velx = 0.02f; // 20mm/s nozzle velocity
    }
    vel[0] = velx; // assign x velocity to mesh boundaries
    Message ("time = % f, vel [0] = % f \n", time , vel [0] ) ; // for debugging purposes
}

```

Appendix 2. Two layer UDF

```

include "udf.h"
include ;math.h;
DEFINE_CG_MOTION(moveNozzle, dt, vel, omega, time, dttime)
{
    /* get the current simulation time */
    float t = RP_Get_Real ("flow-time");
    /* set the printing parameters */
    float print_speed = 0.02f; /* 20mm/s printing speed */
    float layer_thickness = 0.00038f; /*0.38mm layer thickness */
    float layer_length = 0.004f; /*4mm long layer */
    float layer_time = layer_length / print_speed; /* time to print one layer */
    float rise_time = layer_thickness / print_speed;
    float move_time = 0.03; //hold nozzle still so flow can leave the nozzle with moving
    /* calculate the current layer number */
    if (time < move_time) { // hold nozzle still
        vel[0] = 0;
    }
    time = time - move_time; // only in positive time will motion occur
    int layer_num = (int)floor (time / layer_time); // calculate layer number based on time
    //changes direction of x motion based on layer number
    if (layer_num % 2 == 0 && time > 0) {
        vel[0] = print_speed;
    }
    else if (time > 0) {
        vel[0] = -print_speed;
    }
    // used to change the nozzle height for printing of multiple layers
    if (time >= (layer_time*layer_num) time <= ((layer_time+rise_time) * layer_num) layer_num<=1)
        vel[0] = 0;
        vel[1] = print_speed;
        Message ("Changing nozzle height to : %f \n", layer_num * layer_thickness ) ;
    }
    else{
        vel[1] = 0;
    }
    // for debugging and monitoring
    Message ("Layer number : %d\n" , layer_num ) ;
    Message ("Layer time : %f \n", layer_time ) ;
    Message ("Current time : %f \n\n", time ) ;
}

```

Appendix 3. Ramped bed UDF

```

include "udf.h"
include ;math.h;
static real velx=0.0;
static real vely=0.0;
static real omegaz = 0.0;
DEFINE_CG_MOTION(box,dt,vel,omega,time,dttime)
{
    float t = RP_Get_Real("flow-time");
    /* set the printing parameters */
    float print_speed = 0.02f; /* 20mm/s printing speed */
    float rotate_speed = 15; //rad/s
    float part_1_length = 0.0021359f;
    float part_1_time = part_1_length / print_speed; /* time to print one layer */
    float part_2_length = 0.004f; /*4mm long layer */
    float part_2_height = 0.00161f;
    float angle = asin(part_2_height / part_2_length);
    float part_2_time = (part_2_height / sin(angle)) / print_speed;
    float rotate_time = angle / rotate_speed;
    float part_3_length = 0.00323f;
    float part_3_time = part_3_length / print_speed;
    float hold_time = 0.018f; //hold nozzle still so flow can leave the nozzle with moving
//hold nozzle
    if (time >= hold_time) {
        velx = 0;
        vely = 0;
        omegaz = 0;
    }
//move x-axis
    else if (time >= part_1_time + hold_time) {
        velx = print_speed;
        vely = 0;
        omegaz = 0;
    }
//move up ramp
    else if (time >= part_1_time + part_2_time + hold_time) {
        velx = print_speed * cos(angle);
        vely = print_speed * sin(angle);
        if (time >= part_1_time + rotate_time + hold_time) {
            omegaz = rotate_speed; //omit if rotation is not required
            //omegaz = 0; omit for rotation
        }
        else {
            omegaz = 0;
        }
    }
//move straight
    else if (time >= part_1_time + part_2_time + part_3_time + hold_time) {
        velx = print_speed;
        vely = 0;
        if (time >= part_1_time + part_2_time + rotate_time + hold_time) {
            omegaz = -rotate_speed; //omit if rotation is not required
            //omegaz = 0; // omit for rotation
        }
        else {
            omegaz = 0;
        }
    }
    else {
        velx = 0;
        vely = 0;
    }
}

```

```

        omegaz = 0;
    }
    vel[0] = velx;
    vel[1] = vely;
    omega[2] = omegaz; //angular velocity
    Message ("time = %f , vel [0] = %f, vel [1] = %f , omega [3] = %f \n", time, vel [0], vel [1],
}

```

Appendix 4. Cross-WLF UDF

```

include "udf.h"
include "math.h"
DEFINE_PROPERTY(cross_wlf_viscosity, c, t)
{
    float temp=0; // Temperature
    float Tref = 0; // Temperature reference
    float zero_shear; // zero shear viscosity
    float tau; // critical stress
    float n; //power law
    float shear_rate=0; // shear rate
    float D1, D2, D3, A1, A2; // Cross-WLF model parameters
    float viscosity=0; // Calculated viscosity
    //viscosity limits
    real viscous_limit = 5000; //pa.s
    // Cross-WLF parameter
    D1 = 3317190000;
    D2 = 373.15;
    D3 = 0;
    A1 = 20.194;
    A2 = 51.6;
    n = 0.25;
    // Define Cross-WLF model parameters
    Tref = D2; // Reference temperature [K]
    tau = 100861; //critical stress level at the transition to shear thinning
    // Calculate viscosity using Cross-WLF model
    shear_rate = C_STRAIN_RATE_MAG(c, t);
    //checks to ensure shear rate is a number (to prevent potential null values being used)
    if (isnan(shear_rate))
    {
        Message ("shear_rate null:%f \n", shear_rate );
        shear_rate = 1; //sets value to 1 in event of nan
    }
    temp = C_T(c, t);
    if (isnan(temp))
    {
        Message ("temp null:%f \n", temp );
        temp = 273.15; //sets value to 0 degrees in event of nan
    }
    float zero_temp = exp(-(A1 * (temp - Tref)) / (A2 + (temp - Tref)));
    zero_shear = D1 * zero_temp;
    float power = 1 + powf(((zero_shear * shear_rate) / (tau))), (0.75));
    viscosity = zero_shear / power;
    //for debugging purposes
    //Message("power: //Message("zero_shear: //Message("viscosity:
    //checks to ensure value assigned is a number (to prevent potential null values being assigned)
    if (isnan(viscosity)) {
        Message ("viscosity null, setting to 1000:\n", viscosity) ;
        viscosity = 1000; //sets value to 1000 pas in event of nan
    }
}

```

```
    if (viscosity > viscous_limit) viscosity = viscous_limit; //if exceed assigned viscosity limit set value  
to viscous limit (upper limit)  
    if (viscosity < 20.0) viscosity = 20.0; } // lower limit of viscosity  
    return viscosity;  
}
```